1 **Observations and numerical simulation of the effects of the 21**

2 **August 2017 North American total solar eclipse on surface**

3 **conditions and atmospheric boundary-layer evolution**

4

5 **Michael S. Buban • Temple R. Lee • Edward J. Dumas • C. Bruce Baker • Mark Heuer**

6

8 **Abstract**

9 We present unique observations of a total solar eclipse from a small unmanned aircraft system

10 (sUAS) platform that was operated during the 21 August 2017 North American solar eclipse. The

11 observations were collected near Ten Mile, Tennessee, where eclipse totality lasted 2 min 38 s. A

12 2-m micrometeorological tripod was erected on-site to measure surface and air temperature, near-

13 surface water vapour, incoming and outgoing shortwave and longwave radiative fluxes, and

14 turbulent fluxes. The sUAS platform and micrometeorological tripod observations indicate

15 significant cooling below a height of 50 m above ground level (a.g.l.) during and shortly after

16 totality. Near-surface temperatures do not return to pre-eclipse values until about 60 min following

17 totality. Above about 50 m a.g.l., smaller temperature changes are observed during the eclipse, as

18 the duration of the eclipse had less influence on deeper boundary-layer turbulence. Additionally,

19 the sensible heat flux becomes slightly negative around totality, and the turbulence kinetic energy

20 and vertical velocity variance concurrently decrease. The evolution of the near-surface

21 meteorological fields

22

Dr. Michael Buban • Dr. Temple R. Lee
Cooperative Institute for Mesoscale Meteorological Studies (CIMMS) and NOAA/OAR/ARL Atmospheric
Turbulence and Diffusion Division, Oak Ridge, Tennessee, 37830, USA
e-mail: Michael.buban@noaa.gov

Mr. Edward Dumas • Mr. Mark Heuer
Oak Ridge Associated Universities, Oak Ridge, Tennessee, 37830, USA

Dr. C. Bruce Baker
NOAA/OAR/ARL Atmospheric Turbulence and Diffusion Division, Oak Ridge, Tennessee, 37830, USA

23 are investigated in more detail using a large-eddy simulation (LES) model. The simulations
24 generally reproduce the observations well, in terms of the timing and magnitude of changes in
25 temperature, moisture and sensible and latent heat fluxes. However, the LES model slightly
26 underestimates the diurnal range and decrease in temperature during the eclipse while
27 overestimating the sensible heat fluxes.

28

31

1 Introduction

33 Although total solar eclipses occur several times a year around the globe, they are a relatively rare
34 phenomenon at any given point on the Earth's surface. At totality, only diffuse shortwave radiation
35 is incident upon the Earth's surface, and conditions on Earth resemble those just after (prior to)
36 sunset (sunrise). This decrease in incoming shortwave radiation can have a marked effect on the
37 surface radiation balance and the structure of the lower atmospheric boundary layer (ABL).
38 Previous studies have examined the effect of both partial and total solar eclipses on near-surface
39 conditions, with many studies showing surface temperature decreases from 2 - 5°C (e.g., Anderson
40 et al. 1972; Segal et al. 1996; Foken et al. 2001; Founda et al. 2007; Mauder et al. 2007; Lee et al.
41 2018) up to as much as 10°C (Stewert and Rouse 1974). Decreases in both the sensible heat flux
42 (H) and latent heat flux *(LE)* have also been noted. For example, Eaton et al. (1997) and Mauder
43 et al. (2007) found both sensible and latent heat flux values decreasing to zero during the minimum
44 in solar radiation. Decreases in near-surface wind speeds have also been observed during totality
45 (e.g., Anderson and Keefer 1975; Subrahamanyam et al. 2011; Turner et al. 2018).

46 On 21 August 2017, several meteorological instruments were deployed near Ten Mile,
47 Tennessee, USA, to observe a total solar eclipse; the entire eclipse lasted for 2 h 55 min, with the
48 total eclipse lasting for 2 min 38 sec. Unlike previous studies that used conventional
49 meteorological instrumentation, the present study combines measurements from a
50 micrometeorological tripod with measurements from a small unmanned aircraft system (sUAS)
51 platform so as to investigate the temporal evolution of surface and near-surface atmospheric
52 conditions. To further interpret the results, a large-eddy simulation (LES) model was used, and
53 results compared to observations.

54

2 Measurements

The study site was located near Ten Mile, Tennessee, approximately 75 km south-west of

Knoxville (Fig. 1). At the site, a 2-m tripod was installed with an aspirated platinum resistance

58
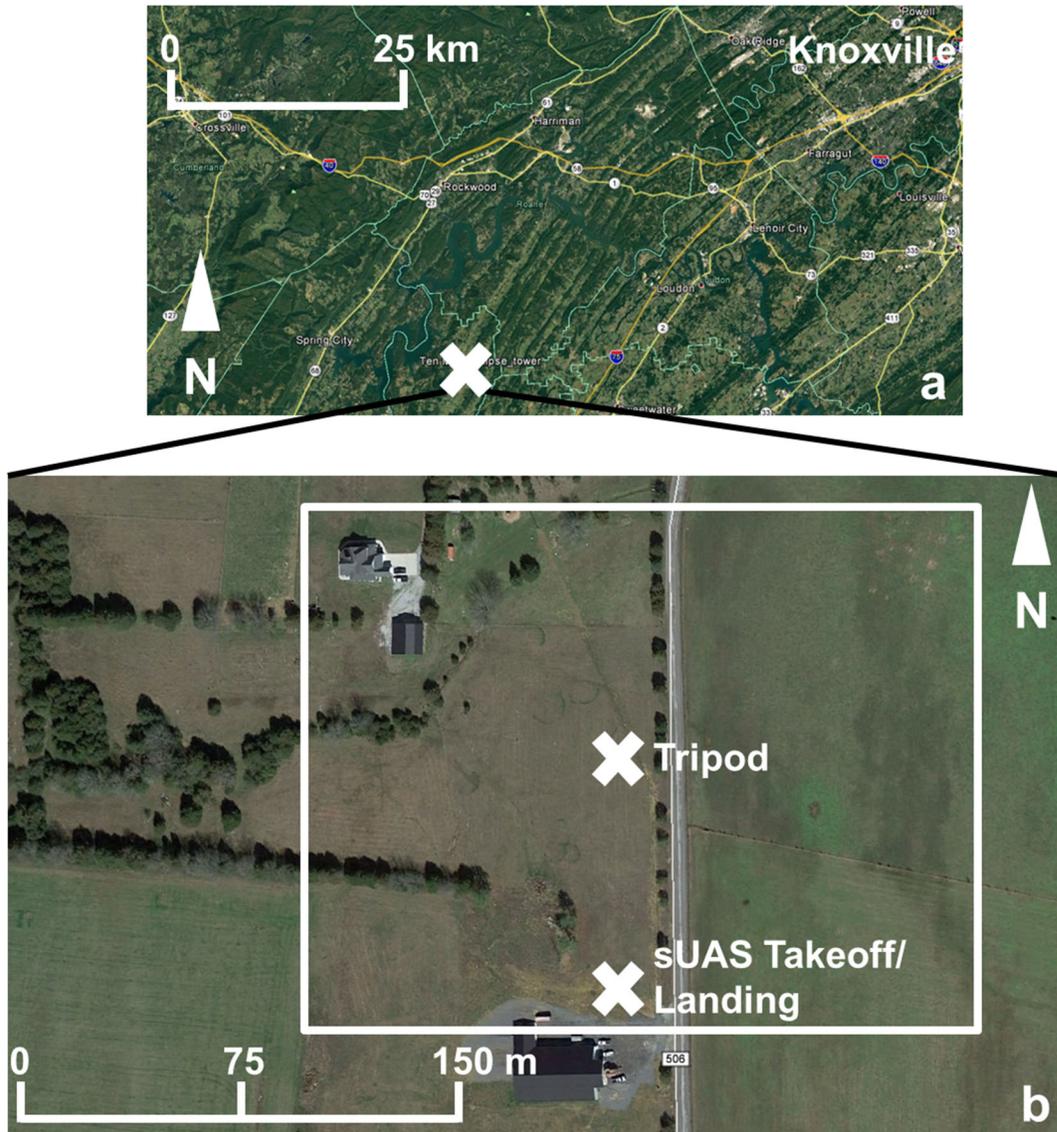
Fig 1 Location of the study site relative to Knoxville, Tennessee (panel a). Panel (b) shows a zoomed in map of study

site, with the locations of the sUAS takeoff and landing noted relative to the instrumented 2-m tripod. White box in

panel (b) indicates the approximate area shown in Figs. 7 and 8. Images are courtesy of GoogleEarth.

62 thermometer, infrared thermometer for measuring land-surface temperature, a net radiometer to

63 measure incoming and outgoing radiation components, a sonic anemometer to determine heat and

64 turbulent fluxes, and an infrared gas analyzer to measure water vapour concentration from which

65 latent heat fluxes could be derived.

66   In addition to these surface and near-surface atmospheric measurements, a DJI S-1000

67 sUAS platform (DJI, Shenzhen, Guangdong, China) was operated; details on the DJI S-1000 sUAS

68 platform are discussed in Dumas et al. (2016) and Lee et al. (2017). Two iMet-XQ sensors

69 (International Met Systems Inc., Kentwood, Michigan, USA), were mounted on top of the sUAS

70 platform to measure temperature and pressure at 1 Hz. The iMet-XQ sensors have a manufacturer-

71 stated accuracy of $\pm$ 0.3°C and $\pm$ 1.5 hPa for temperature and pressure, respectively (e.g., Lee et

72 al., 2017). The sUAS platform flew up to a height of 365 m above ground level (a.g.l.) to

73 characterize the ABL temperature evolution. On the underside of the sUAS platform was a

74 downward-pointing FLIR Tau 2 infrared camera (FLIR Systems Inc., Wilsonville, Oregon, USA)

75 comprising a 7.5-mm lens with a 45° view angle and 336 × 256 pixel resolution and able to

76 measure surface temperature at 1 Hz (Dumas et al. 2016).

77   A total of eight flights were flown on 21 August; four flights were made prior to totality

78 (at 150 min, 90 min, 60 min, and 30 min prior to totality), and three flown after totality (at 30 min,

79 60 min, and 90 min after totality) with an average flight time of approximately 12.5 min (Table 1).

80 An additional flight was flown about 5 min prior to totality. During all of these flights, the sUAS

81 platform hovered at 365 m a.g.l. above the tripod for 2 - 4 min to sample changes in air temperature

82 and land-surface temperature.

83

84 **3. Numerical model**

85 The Large-eddy simulation (LES) model was used based on the Collaborative Model for

86 Multiscale Atmospheric Simulation or COMMAS (e.g., Wicker and Wilhemson 1995; Coniglio et

87 al. 2006; Buban et al. 2012) and simulations compared with observations collected during the

88 eclipse. The COMMAS model is a cloud-resolving and non-hydrostatic model that includes a

89 weakly-diffusive fifth-order horizontal advection scheme (Wicker and Skamarock 2002), a third-

90 order vertical advection scheme, a 1.5-order parametrization for turbulent kinetic energy, and a

91 modified force-restore land-surface–atmosphere exchange scheme (Deardorff 1978; Peckham et

92 al. 2004; Buban et al. 2012). Within this scheme the surface was treated as horizontally

4

93　homogeneous and the simulations u a horizontal grid spacing of 100 m. To capture the rapid low-
94　level evolution of the ABL during the total eclipse, the lowest 25 grid levels had a vertical spacing
95　of 6 m, with the lowest model level at 3 m a.g.l. Above 150 m, the grid was stretched, culminating
96　in a grid spacing of 50 m at the top of the domain. The domain size was $36 \times 36 \times 6$ km for the x,
97　y, and z dimensions, respectively, and periodic lateral boundary conditions were applied. The
98　model was initialized using the 0800 LDT (local daylight time = UTC – 4 h) sounding from
99　Nashville, Tennessee, which is located approximately 200 km west of the Ten Mile site (Fig. 2).
100　Nashville was the nearest sounding site, and conditions were synoptically homogeneous over the
101　entire region. The simulation was run for 12 h covering the daylight period following the sounding
102　launch.
103

104
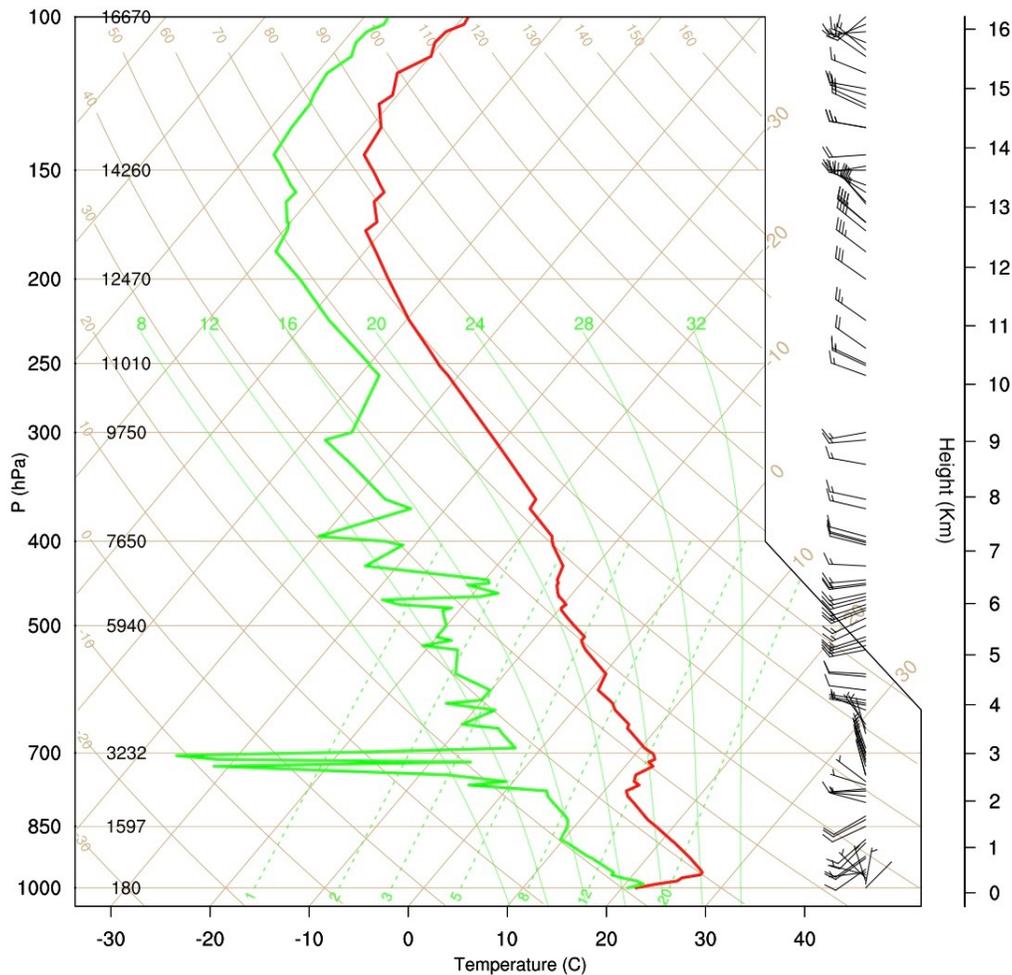
105　**Fig 2** Skew-T diagram of temperature (red line), and dewpoint temperature (green line) at 0800 local daylight time
106　(1200 UTC) 21 August 2017 at Nashville, Tennessee.

5

107

4 Results

4.1 Pre-eclipse conditions

Early morning conditions were fairly quiescent over the mid-south USA, as represented by the
Nashville sounding (Fig. 2). A low-level inversion had set up with saturated conditions near the
surface and dew covering the ground with, patches of fog scattered throughout the area. Above
the surface, drier air found with low wind speeds throughout the depth of the troposphere.
Throughout the morning and into the afternoon, surface and 1.5-m temperatures gradually
increased by about 10° C, and 1.5-m dewpoints decreased by about 4° C as the vertical
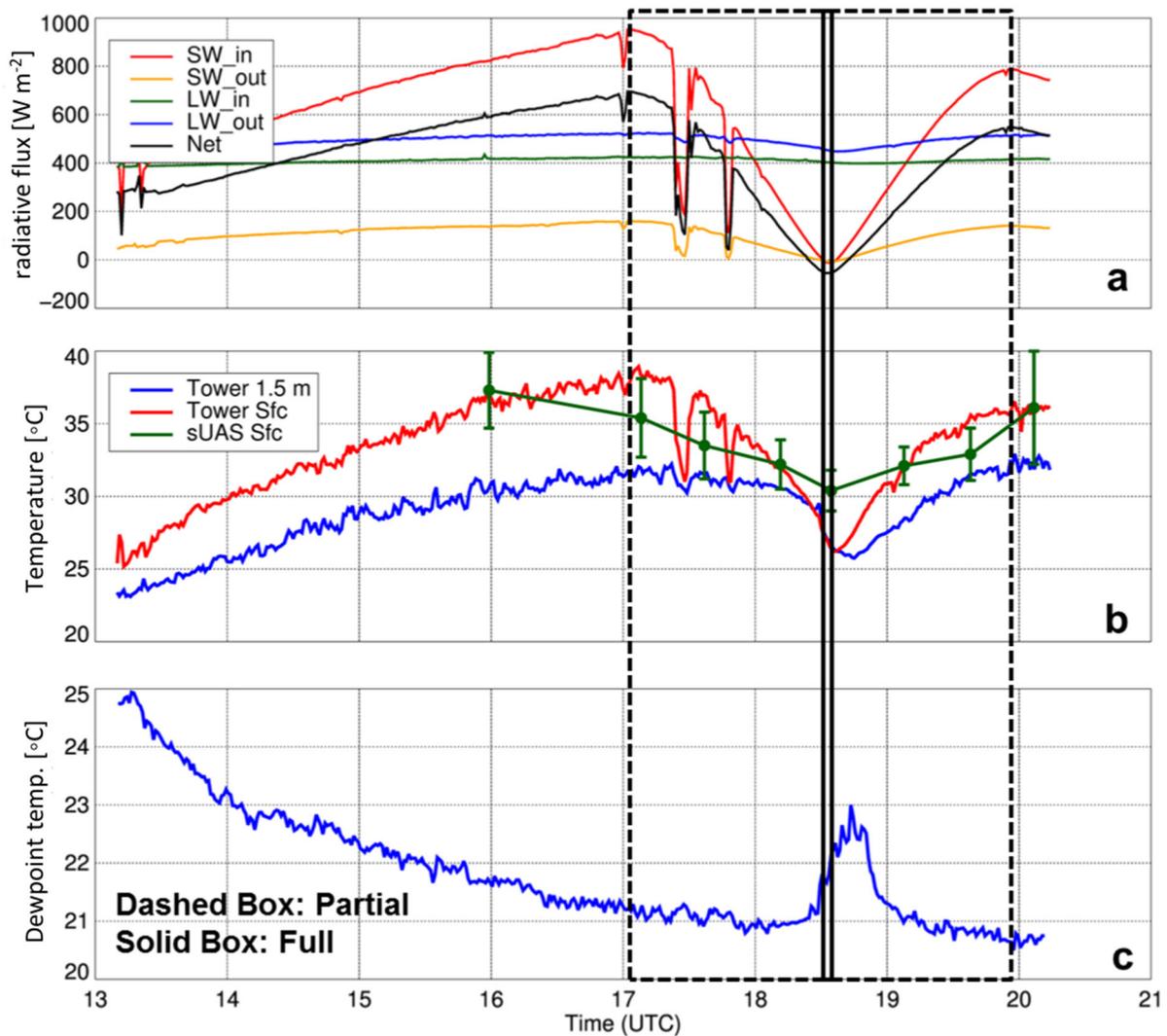
Fig 3 Radiative flux components during daytime on 21 August 2017 (a). Red, orange, green, blue, and black lines
show incoming shortwave radiative flux, outgoing shortwave radiative flux, incoming longwave radiative flux,

outgoing longwave radiative flux, and net radiative flux, respectively. Panel (b) shows surface temperature (red line), air temperature measured 1.5 m a.g.l. (blue line), and surface temperature (filled circle) and standard deviation (vertical bars) measured from the sUAS platform (green) whereas panel (c) shows dewpoint temperature. 1-min means are used in all analyses. The dashed black box denotes the eclipse period with the solid vertical lines depicting the period of totality.

mixing and ABL growth commenced (Fig. 3). Similar low-level ABL warming and drying is also seen in the LES model results (Fig. 4), however the magnitudes of these changes are slightly lower. One consideration is that the lowest model level is at 3 m a.g.l. and therefore would be expected to have smaller changes than at the 1.5-m observation level. Additionally, the simulation had a cool bias in the temperatures and a dry bias in the dewpoints. By early afternoon, the lower atmosphere developed ABL-topped cumuli as lifted condensations levels were achieved, as indicated by the sharp decreases in incoming shortwave radiation (Fig. 3a). ABL-topped cumuli also developed in the LES model by early afternoon (Fig. 5a).
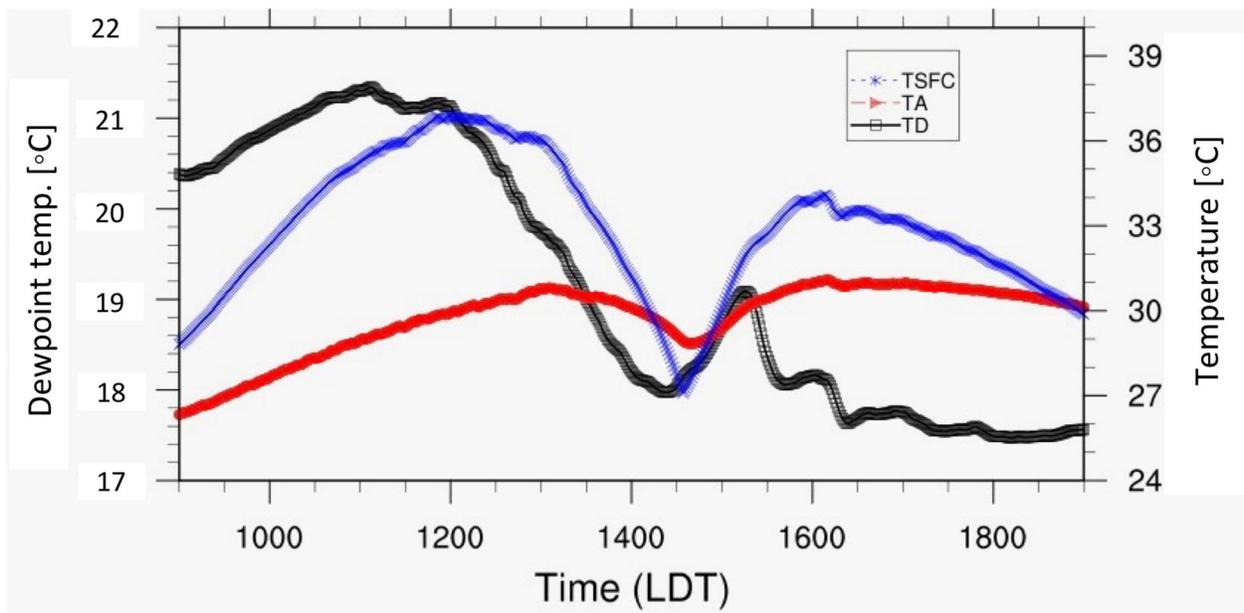
Fig 4 Surface temperature (blue line), 3 m air temperature (red line), and 3 m dewpoint (black line) from the simulation.

4.2 Conditions during the eclipse

The partial eclipse began at 1303:37 local daylight time, with totality lasting from 1432:07 through 1434:46 local daylight time, and ended at 1558:13 local daylight time over the study site. As the

141 partial eclipse began, the incoming shortwave radiative flux decreased from ≈ 900 W m^{-2} to zero

142 during totality (Fig 3a). After totality, the shortwave radiative flux steadily increased to ≈ 800 W

143 m^{-2}. The outgoing shortwave radiative flux showed an immediate response, decreasing to zero

144 during totality. Note the sharp localized decreases in incoming and outgoing shortwave and net

145 radiative fluxes as clouds passed over the site.

146 　　　The outgoing longwave radiative flux showed a decrease during the eclipse period, with a

147 smaller, decrease ≈ 100 W m^{-2} during the event. The incoming longwave radiative flux showed a

148 very slight decrease; however, the longwave radiative flux components showed a time lag, with

149 minimum values just after totality ended. The temperatures showed a decrease during the eclipse

150 with the surface temperature decreasing by ≈ 12 °C and 1.5-m temperatures decreasing by ≈5 °C

151 (Fig. 3b). There was a time lag in the temperature changes as minimum values occurred just after

152 totality ended with a greater lag in the 1.5-m temperature (≈ 13 min) compared to the surface

153 temperature (≈ 4 min). Both temperatures then steadily increased as the eclipse continued.

154
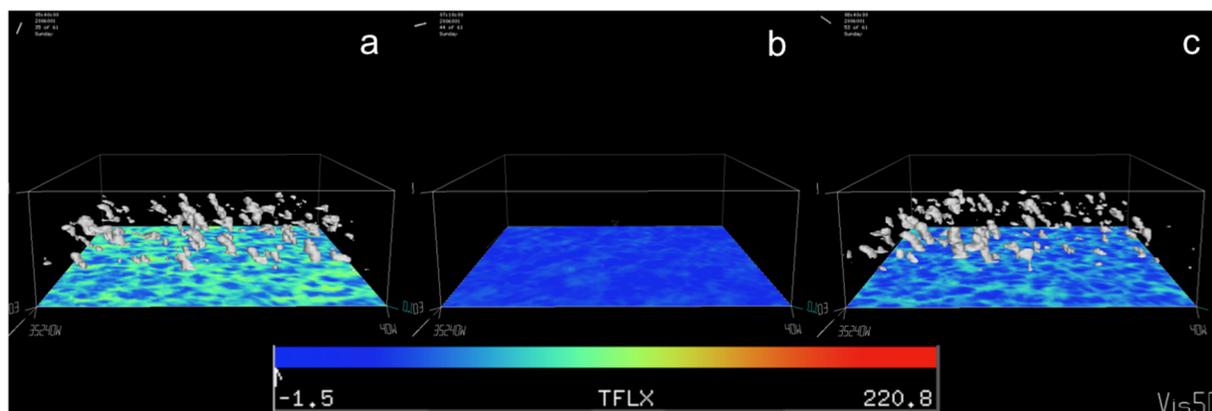
156 **Fig 5** Surface sensible heat flux (color filled) and cloud water content > 0.05 g kg^{-1} (white surfaces) at 1340, 1510,

157 and 1640 LDT.

158

159 　　　Results from the simulation parallel those of the observations with surface temperatures

160 decreasing ≈ 9 °C and 3-m temperatures decreasing by ≈1.5 °C (Fig. 4). The decrease in

161 temperatures is consistent with the bias of a smaller diurnal increase in temperatures in the model

162 prior to the eclipse. The simulated temperatures also show a time lag in the minima, with the 3-m

163 temperature lag greater (≈ 5 min) than the surface temperature lag (≈ 1 min). These time lags are

164 smaller than observed.

165   c
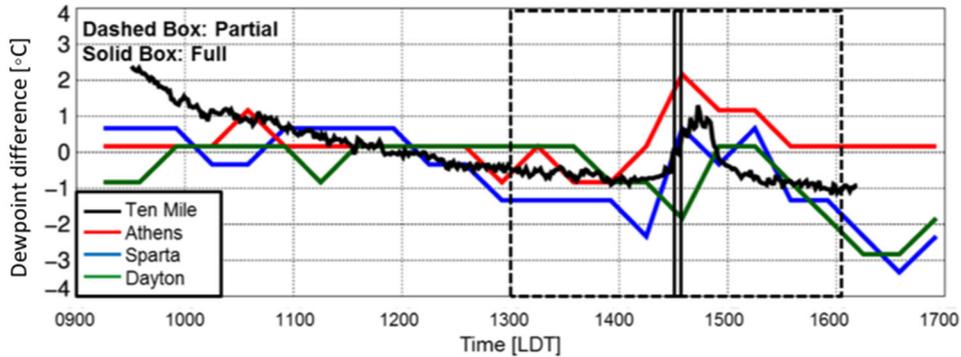
166
167   **Fig 6** Time series of dewpoint temperature with the mean value between 1100 and 1300 LDT subtracted at three
168   sites in eastern Tennessee compared with observations from Ten Mile. Athens is approximately 25 km south-east of
169   Ten Mile; Sparta is about 80 km north-west of Ten Mile; and Dayton is 35 km to the south-west.

170

171   The observed dewpoint temperature showed an interesting steady decrease at a rate similar
172   to before the eclipse began until just prior to the start of totality when it spiked higher by $\approx 2\ °C$,
173   peaking after totality ended, then decreasing rapidly until the middle part of the partial phase before
174   steadily decreasing thereafter (Fig. 3c). This feature was also found in the LES model, where
175   approximately a 3 °C dewpoint increase developed with the increase lasting longer in the
176   simulations than the observations. These moisture profiles were also seen at three other nearby
177   sites that were in the path of totality (Fig. 6). Each of these sites experienced an increase in
178   dewpoint temperature by $\approx$ 2-3 °C for about 30 min before decreasing to below pre-eclipse values.

9
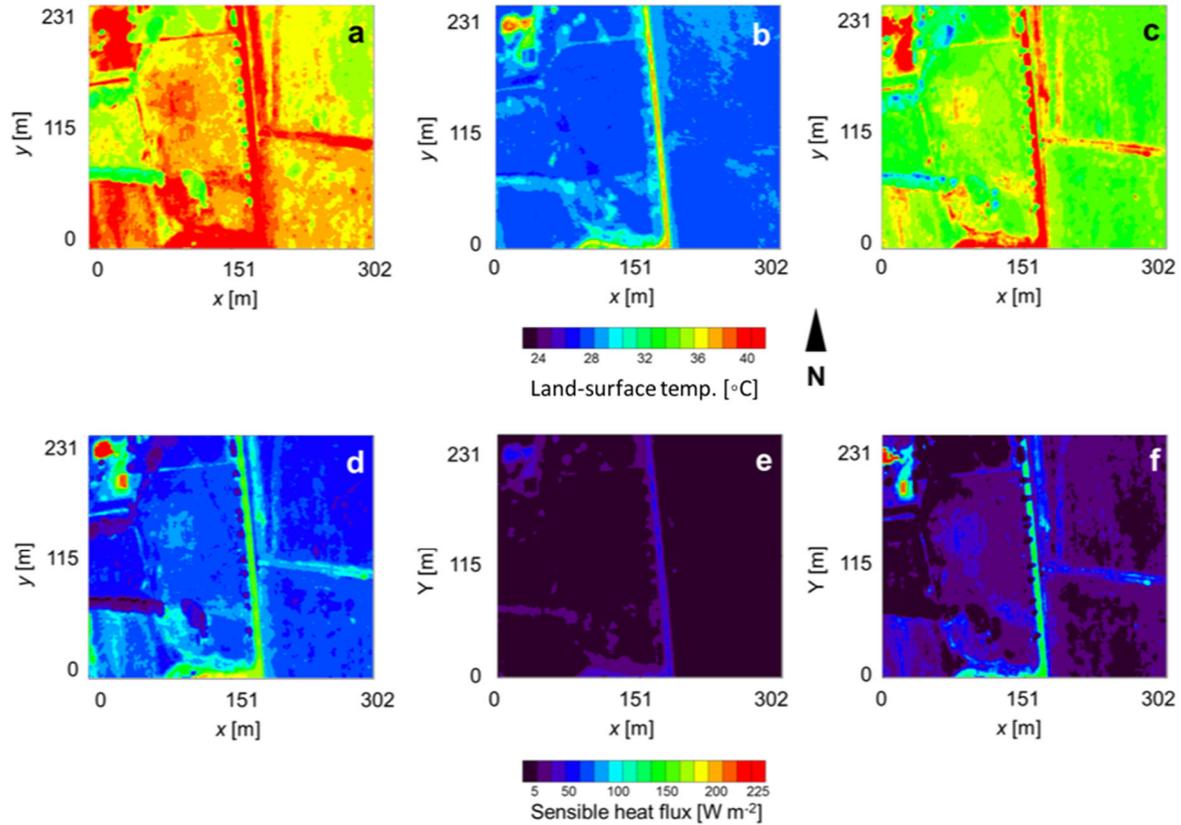
Fig 7 Land-surface temperatures measured with the FLIR infrared camera onboard the sUAS platform at 1308:41 LDT (panel a), 1432:28 LDT (panel b), and 1606:23 LDT (panel c). Surface sensible heat flux computed from the sUAS platform are shown in panels d-f and correspond with the times shown in panels a-c.

Changes in land-surface temperature were further examined using measurements from the FLIR infrared camera mounted on the sUAS platform. From the start of the eclipse until totality, a decrease of about 9 °C was observed (Figs. 7a-b), with a subsequent rise of about 7 °C from just after the end of totality until the end of the eclipse (Figs. 7b-c). This result is more consistent with the model values than the point observations as model results were horizontally averaged. From 1 min prior to totality to 40 s before the end of totality land-surface temperature decreased by about 1°C (Figs. 8a, b), then by approximately 80 s after totality, the land-surface temperature over the area had increased by about 1.5 °C (Figs. 8b, c) as sunlight returned. Note that the surface temperatures in Fig. 8c are lower than in Fig. 8a, indicative of the temperature lag as seen in the tripod observations.
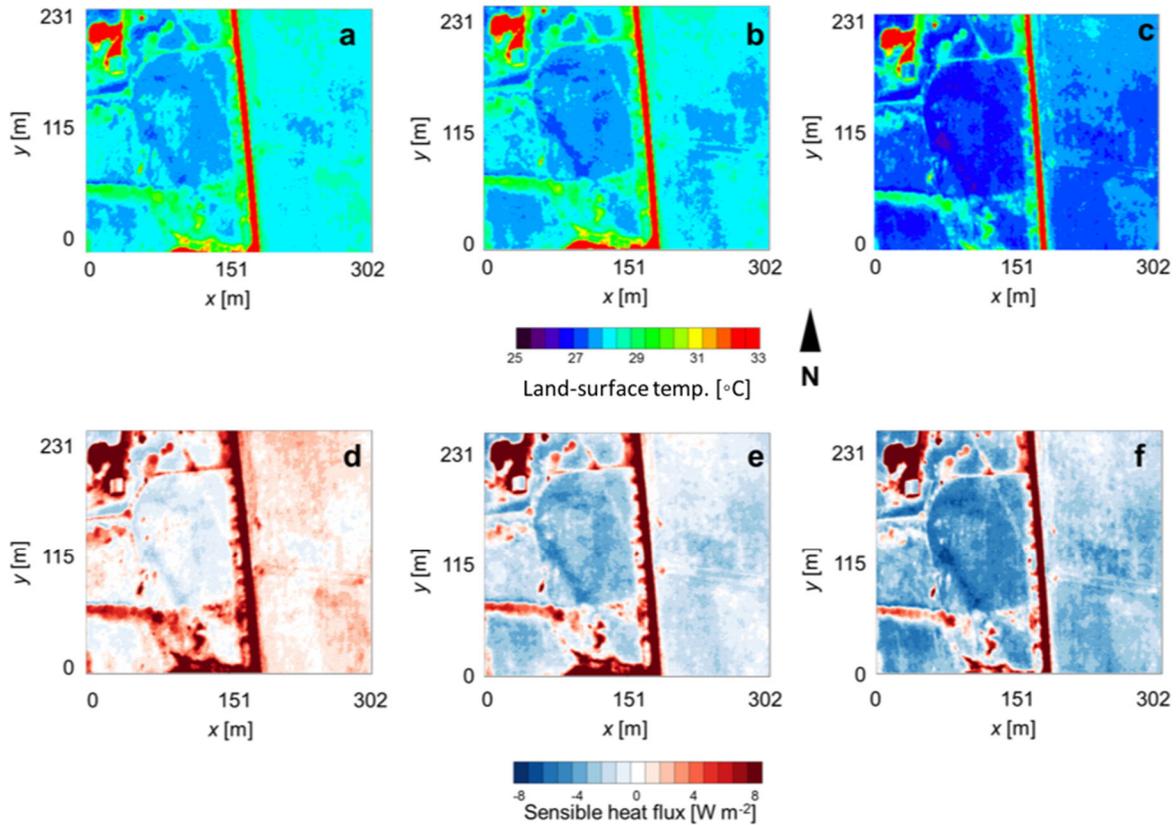
Fig 8 Land-surface temperatures measured with the FLIR infrared camera onboard the DJI S-1000 (panels a-c) and corresponding surface sensible heat flux (panels d-f) at 1431:06 LDT (left), 1434:06 LDT (middle) and 1436:06 LDT (right).

The sensible heat flux also showed a decrease during the eclipse, decreasing from ≈100 W m^{-2} to about –5 W m^{-2} just prior to totality before increasing towards the end of the partial phase of the eclipse as measured at the tripod (Fig. 9a). The latent heat flux showed a larger decrease from ≈ 300 W m^{-2} to about –25 W m^{-2} with a slight lag compared to the sensible heat flux. The sensible and latent heat fluxes in the LES model compare well with the observations in terms of magnitudes and timing of the flux decreases, however there is a large bias in the latent heat flux (Fig. 10). The spatial structure in the sensible heat flux was also computed using tripod data in conjunction with the sUAS platform land-surface temperature (Figs. 7, 8d-f) as in Lee et al. (2017) during the periods that the sUAS platform hovered at 365 m a.g.l. The computed sensible heat fluxes decreased by ≈100 – 150 W m^2 to near zero during totality, before increasing by about 100 W m^2 at the end of the eclipse. Similar patterns were seen in the modelled turbulent kinetic energy

213   ($\bar{e}$) and vertical velocity variances (Fig. 9b); however these two variables reached a minimum

214   during the period of totality.
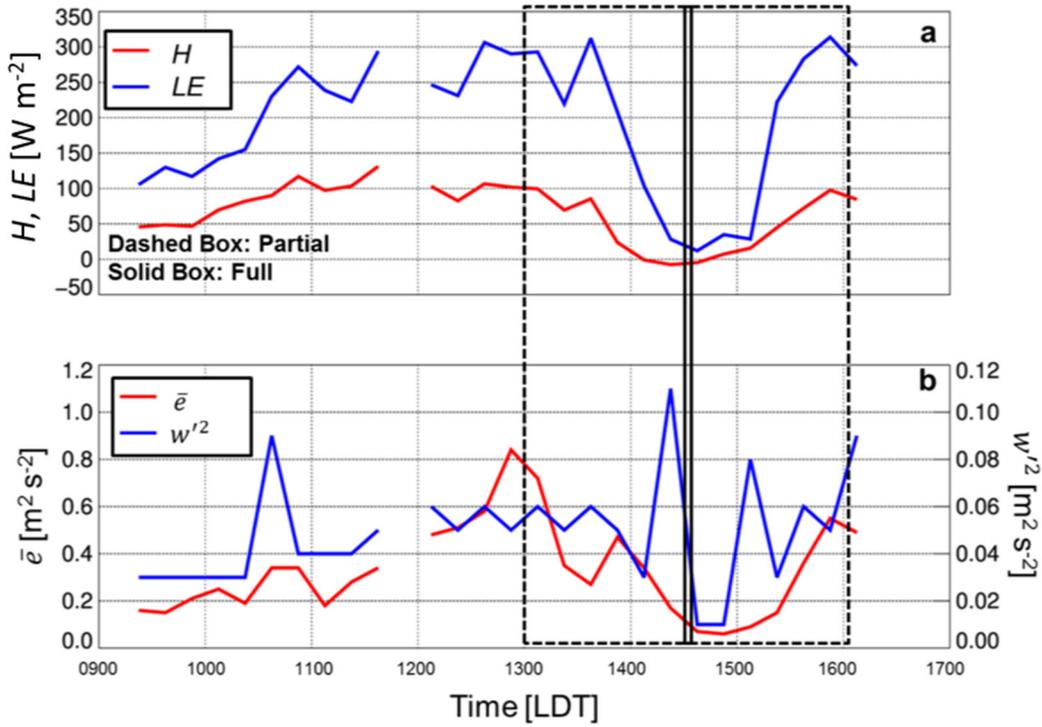
215
216   **Fig 9** Sensible ("H", red line) and latent ("LE", blue line) heat flux (panel a). Panel (b) shows the $\bar{e}$ (red) and vertical

217   velocity variance (blue). The dashed black box denotes the eclipse period, and the solid vertical lines depict the period

218   of totality.

219
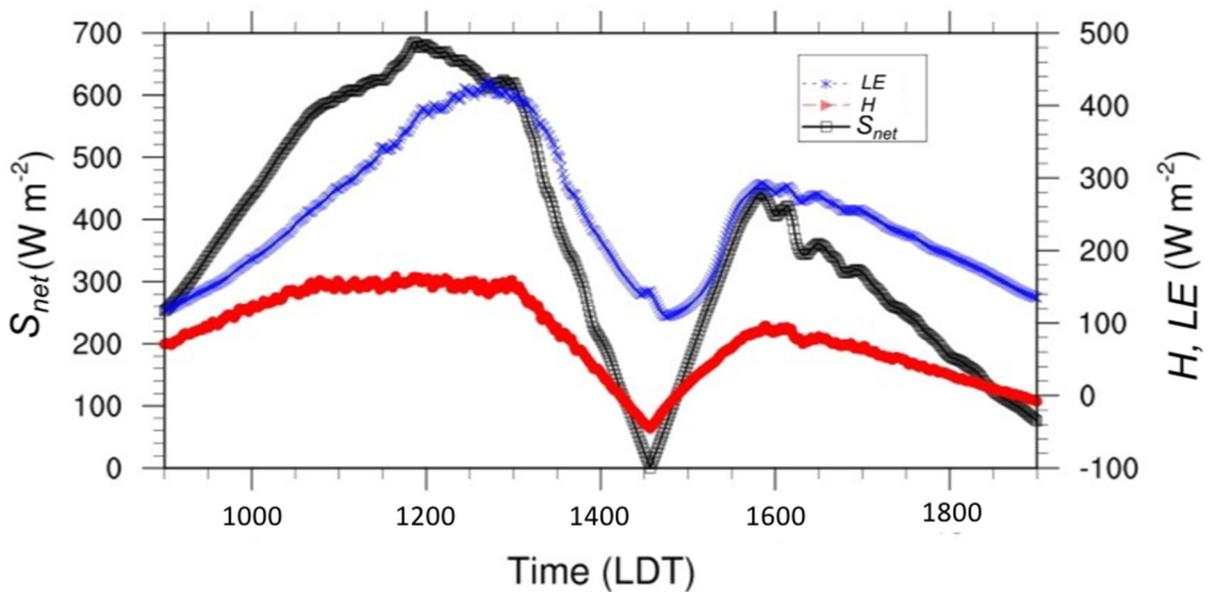
220

221 **Fig 10** Net shortwave radiative flux ("SWNET", black), sensible heat flux (red), and latent heat flux (blue) from the
222 simulation.
223
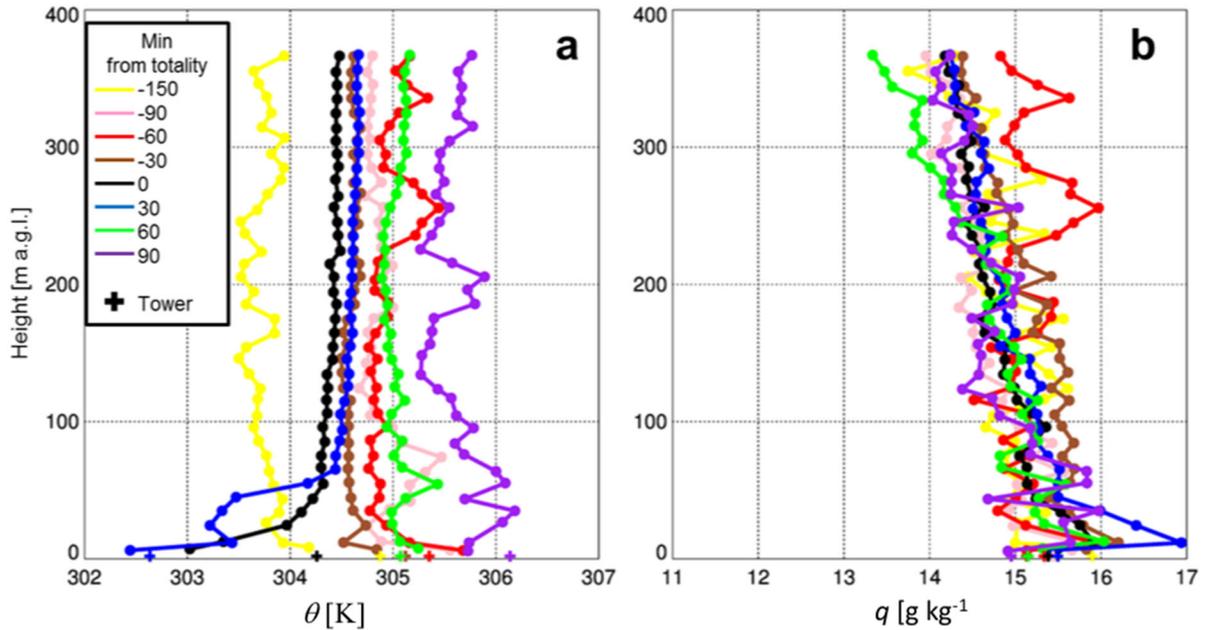
224
225 **Fig 11** Vertical profiles of potential temperature (left) and specific humidity (right) obtained from the sUAS platform
226 during eight separate flights prior to, after, and during the eclipse. Each color is an individual flight as noted in the
227 legend. Data averaged into 10-m bins. Mean tripod measurements during each flight are shown by a "+."
228

229   The profiles of temperature between the surface and 365 m a.g.l. obtained from the sUAS
230 platform prior to the eclipse showed the development of a superadiabatic near-surface layer (Fig.
231 11a), and by 30 min prior to the start of totality, the superadiabatic near-surface layer became
232 neutrally stratified The flight that began 2 min prior to the start of totality and the flight 30 min
233 after totality ended exhibited a near-surface inversion, with inversion strength peaking at ≈1.5 - 2
234 °C, with a vertical extent of about 50 m. The flights 60 min and 90 min following totality, however,
235 showed the redevelopment of a neutral near-surface layer towards the end of the partial eclipse
236 (Fig. 11a). Farther aloft, we observed a neutral layer that slowly warmed before and during the
237 first part of the eclipse, cooled slightly near the period of totality, and then warmed again as the
238 eclipse ended (Fig. 11a). During the period leading up to totality the vertical profiles from the LES
239 model are consistent with the sUAS platform observations, showing the development of a
240 superadiabatic layer, then a neutral layer, followed by a ≈ 50 m deep inversion (Fig. 12a).
241 However, the strength of the inversion in the simulation was about half that observed by the sUAS

13

242 platform. Also, in the sUAS platform observations, a near-neutral layer developed and persisted,
243 whereas the LES showed redevelopment of the near-surface superadiabatic layer.   The
244 development of the superadiabatic layer in the LES model but not in the observations may have
245 been due to the treatment of the lower boundary condition. In the LES model, the lower boundary
246 was treated as homogeneous, whereas near the observation site, there was significant
247 heterogeneity, both in land-surface conditions and terrain.

248   Measurements of water vapour mixing ratio showed a very gradual drying of the ABL aloft
249 throughout the event; however, near the surface there was a slight increase in moisture just after
250 totality ended, before drying continues (Fig. 11b). The observations are consistent with the tripod
251 observations and observations from nearby sites. Similar results are seen in the simulation with
252 drying occurring up to near the start of totality, then an increase in low-level moisture, before
253 drying commences (Fig. 12b). It should be noted that, in addition to the aforementioned dry bias
254 in the model, the model also produces strong moisture lapse rates just above the surface, which
255 were not measured by the sUAS platform. Since the model used homogenous boundary conditions
256 it is possible that local effects in the field of the observations may have contributed to the dry
257 model bias.
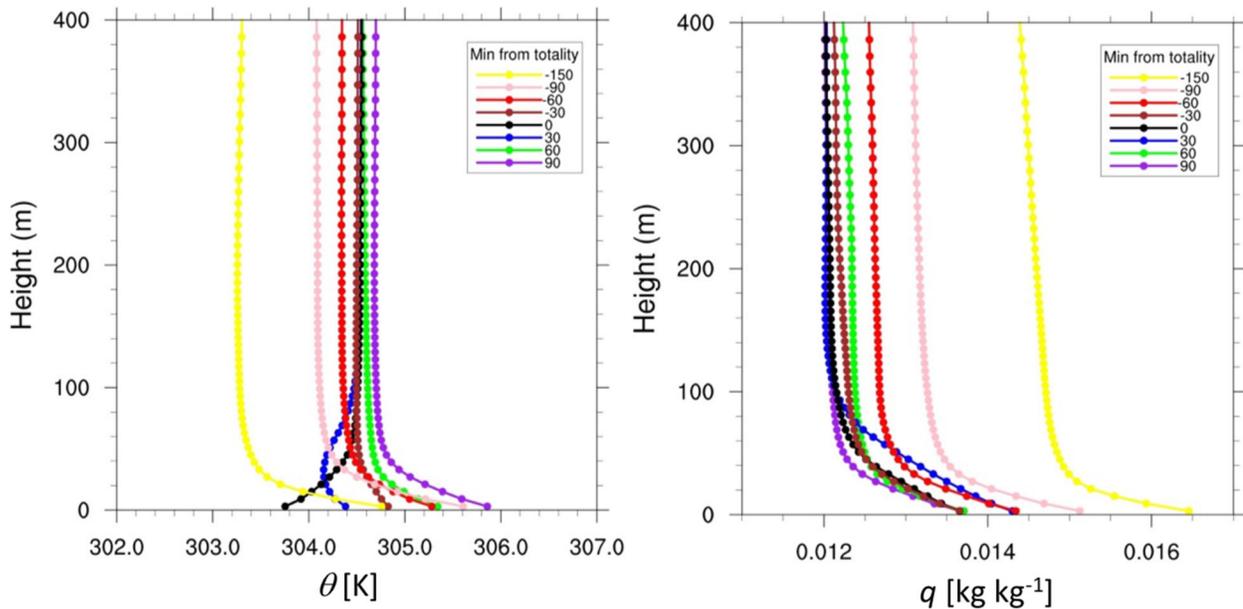
258
259 **Fig 12** Vertical profiles of potential temperature (left) and water vapour mixing ratio (right) from the simulation
260 during eight separate flights prior to, after, and during the eclipse. Each color is an individual flight as noted in the
261 legend

262

263

5 Discussion and Conclusions

We have described the first known observations of air temperature from a sUAS platform during a total solar eclipse on 21 August 2017. These observations allowed us to characterize the evolution of temperature fields between the surface and 365 m a.g.l. We complemented the sUAS platform measurements with surface meteorological and flux observations from a 2-m micrometeorological tripod that was installed near Ten Mile, Tennessee, USA. This site was particularly advantageous because of the long duration (i.e., 2 min 38 s) of eclipse totality and because of the mostly clear, fair-weather conditions that were observed on this day. Also, since the eclipse occurred near the time of peak local heating, this event afforded a unique opportunity to observe the surface and ABL evolution due to rapid changes in shortwave radiation. To complement the observations, a LES model was used, and results compared to the observations, allowing evaluation of model performance under these unique conditions.

276
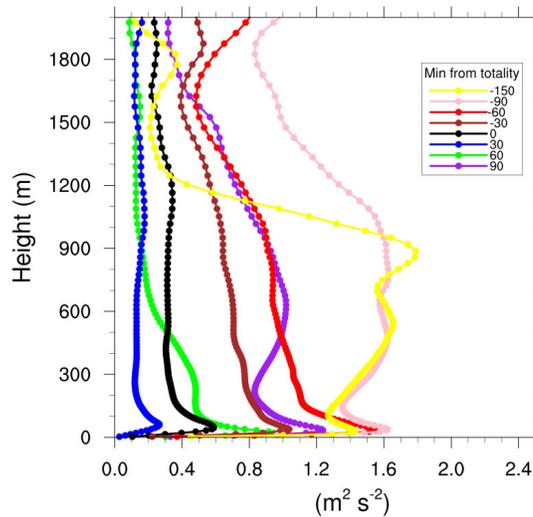
Fig 13 Vertical profile of the $\bar{e}$. Colours represent times as in Fig. 12.

The observations were generally consistent with other studies of partial and total solar eclipses. The primary findings show that, as the incoming shortwave radiative flux decreases to zero, surface and 1.5-m air temperatures also decrease. A time lag in the minimum in surface temperature of ≈ 4 min is consistent with that of 7 min found by Eaton et al. (1997). The 1.5-m

15

284   a.g.l. temperature had a time lag of 13 min and is consistent with the range of values reported in

285   the literature (e.g., Anderson 1999). The time lag is generally longer for temperatures at levels

286   further from the ground, as it takes longer for surface-based conduction/convection to affect these

287   levels. However, the time lag is also dependent on the local atmospheric and surface conditions,

288   such as terrain and vegetation. Values of surface sensible heat flux also decreased to zero,

289   consistent with Eaton et al. (1997), Foken et al. (2001), Mauder et al. (2007), and Turner et al.

290   (2018). Also, *TKE* decreased substantially, as forcing for vertical motion diminished, which was

291   consistent with Krishnan et al. (2004). Vertical profiles of *TKE* from the LES also showed

292   decreases throughout the ABL until just after totality before increasing as the eclipse ended (Fig.

293   13). These decreases are maximized near the middle of the ABL and are less near the ABL top.

294   These results are consistent with those found in simulations of the onset of the nocturnal inversion

295   (e.g., Moeng and Sullivan 1994; Mironov and Sullivan 2016). It is interesting to note that by 60

296   min after eclipse totality low-level *TKE* is increasing, and is still decreasing at a height of ≈1000

297   m a.g.l. By 90 min after eclipse totality, *TKE* is increasing throughout the ABL. This vertical time

298   lag is consistent with *TKE* being driven by surface heating.   It is also notable that there were

299   numerous cumuli atop the ABL prior to the eclipse, which dissipated and led to clear skies during

300   totality; cumuli then redeveloped as the eclipse ended as was observed (not shown). This ABL

301   evolution was reproduced in the simulation (Fig. 5). Also notable was the rapid increase in near-

302   surface dewpoint that occurred just prior to totality, peaking just after totality then decreasing soon

303   after to near pre-eclipse levels. The post-eclipse increase in low-level moisture that was seen at

304   this site and other sites within the path of totality and reproduced in the simulation merits further

305   study.

306   Whereas surface meteorological and flux measurements have been reported during

307   previous total eclipses, vertical profiles through the lower atmosphere have been largely

308   unattainable due to limitations in instrumentation with the exception of Turner et al. (2018) . With

309   the use of the sUAS platform, we have obtained vertical profiles of temperature and moisture

310   before, during, and after the eclipse to provide insight into ABL dynamics during this period. We

311   found substantial cooling in the near surface (≈ 50 m) as the eclipse approached totality, which

312   was followed by recovery as the partial eclipse ended. Above this height, only modest changes

313   were observed, with the timescale of the eclipse having a smaller influence on deeper ABL

314   turbulence around totality. Our observations are consistent with Turner et. al (2018) who observed

16

the partial eclipse at the Atmospheric Radiation Measurement (ARM) site in norther Oklahoma, USA.

The LES model generally reproduced the observations well, in terms of timing and magnitude of changes in temperature, moisture and sensible and latent heat fluxes, although with a few caveats. The model tended to slightly underestimate the diurnal range and decrease in temperature during the eclipse and tended to overestimate the sensible heat flux compared to the point observations. One limitation is that the simulation was run over a homogeneous surface and the results shown are domain averages. Also, the model had a dry bias both near the surface and aloft. Some of these differences might be attributed to using a sounding for initialization that was synoptically representative but was not representative of the local terrain surrounding the Ten Mile area. More importantly, these results, combined with other high-resolution numerical models (e.g., the High-Resolution Rapid Refresh) should be further examined to highlight weaknesses in model parametrizations so that improvements can be made.

References

Anderson J (1999) Meteorological changes during a solar eclipse. Weather 54:207–215

Anderson RC, Keefer DR, Myers OE (1972) Atmospheric pressure and temperature changes during the 7 March 1970 Solar eclipse. J Atmos Sci 29:583–587

Anderson RC, Keefer DR (1975) Observations of the temperature and pressure changes during the 30 June 1973 solar eclipse. J Atmos Sci 32:228–231

Buban MS, Ziegler CL, Mansell ER, Richardson YP (2012) Simulation of dryline misovortex dynamics and cumulus formation. Mon Weather Rev 140:3525–3551

Coniglio MC, Stensrud DJ, Wicker LJ (2006) Effects of upper-level shear on the structure and maintenance of strong quasi-linear mesoscale convective systems. J Atmos Sci 63:1231–1252

Deardorff JW (1978) Efficient prediction of ground surface temperature and moisture, with inclusion of a layer of vegetation. J Geophys Res 83:1889-–1903

349   Dumas EJ., Lee TR, Buban MS, Baker CB (2016) Small Unmanned Aircraft System (sUAS) measurements during
350   the 2016 Verifications of the Origins of Rotation in Tornadoes Experiment Southeast (VORTEX-SE). NOAA
351   Technical Memorandum OAR ARL-273, doi:10.7289/V5/TM-OAR-ARL-273

352   Eaton FD, Hines JR, Hatch WH, Cionco RM, Byers J, Garvey D, Miller DR (1997): Solar eclipse effects observed in
353   the planetary boundary layer over a desert. Boundary-Layer Meteorol 83:331–346

354   Founda DD, Melas, Lykoudis S, Lisardis I, Gerasopoulos E, Kouvarakis G, Petrakis M, Zerefos C (2007) The effect
355   of the total solar eclipse of 29 March 2006 on meteorological variables in Greece. Atmos Chem Phys 7:5543–
356   5553

357   Foken TB, Wichura, Klemm O, Gerchau J, Winterhalter M, Weidinger T, (2001) Micrometeorological measurements
358   during the total solar eclipse of August 11, 1999. Meteorol Z 10:171–178

359   Krishnan PP, Kunhikrishnan K, Muraleedharan S, Nair, Ravindran S, Ramachandran R, Subrahamanyam DB,
360   Venkata Ramana M (2004) Observations of the atmospheric surface layer parameters over a semi arid region
361   during the solar eclipse of August 11th 1999. Proc Indian Acad Sci 113:353–363

362   Lee TR, Buban MS, Dumas E, Baker CB (2017) A new technique to estimate sensible heat fluxes around
363   micrometeorological towers using small unmanned aircraft systems. J Atmos Oceanic Tech 34:2103-2112.

364   Lee TR, Buban MS, Palecki M, Leeper R, Diamond HJ, Dumas E, Meyers T, Baker B (2018) Great American Eclipse
365   data may fine-tune weather forecasts. EOS, in press

366   Mauder M, Desjardins RL, Oncley S, MacPherson I (2007) Atmospheric response to a partial solar eclipse over a
367   cotton field in central California. J Appl Meteorol Climatol Soc 46:1792–1803

368   Mironov D, Sullivan PP (2016) Second moment budgets and mixing intensity in the stably stratified atmospheric
369   boundary layer over thermally heterogeneous surfaces. J Atmos Sci 73:449–464

370   Moeng CH, Sullivan PP (1994) A comparison of shear-and buoyance-driven planetary boundary layer flows. J Atmos
371   Sci 51:999–1022

372   Peckham SE, Wilhelmson RB, Wicker LJ, Ziegler CL (2004) Numerical simulation of the interaction between the
373   dryline and horizontal convective rolls. Mon Weather Rev 132:1792–1812

374   Segal M, Turner RW, Prusa J, Bitzer RJ, Finley SV (1996) Solar eclipse effect on shelter air temperature. Bull Am
375   Meteorol Soc 77:89–99

376   Stewert RB, Rouse WR (1974) Radiation and energy budgets at an arctic site during the solar eclipse of July 10, 1972.
377   Arct Alp Res 6:231–236

378   Subrahamanyam DB, Anurose TJ, Mohan M, Santosh M, Kiran Kumar NVP, Sijikumar S, Prijith SS, Aloystus M
379   (2011) Atmospheric surface-layer response to the annular solar eclipse of 15 January 2010 over
380   Thiruvananthapuram, India. Boundary-Layer Meteorol 141:325–332

381   Turner DD, Wulfmeyer V, Behrendt A, Bonin TA, Choukulkar A, Newsom RK, Cook DR (2018) Response of the
382   land-atmosphere system over north-central Oklahoma during the 2017 eclipse. Geophys Res Lett 45:1668–
383   1675

384   Wicker LJ, Skamarock W (2002) Time-splitting methods for elastic models using forward time schemes. Mon
385   Weather Rev 130:2088–2097

386   Wicker LJ, Wilhelmson RB (1995) Simulation and analysis of tornado development and decay within a three-

387   dimensional supercell thunderstorm. J Atmos Sci 52:2675–2703